Chaofeng Lü
Department of Civil Engineering and
Soft Matter Research Center,
Zhejiang University,
Hangzhou 310058, China;
Department of Civil and Environmental
Engineering and Mechanical Engineering,
Northwestern University,
Evanston, IL 60208

Ming Li
Department of Civil and Environmental
Engineering and Mechanical Engineering,
Northwestern University,
Evanston, IL 60208;
State Key Laboratroy of
Structural Analysis for Industrial Equipment,
Dalian University of Technology,
Dalian 116024, China

Jianliang Xiao[1]
Department of Mechanical Engineering,
University of Colorado,
Boulder, CO 80309
e-mail: Jianliang.Xiao@colorado.edu

Inhwa Jung
Department of Mechanical Engineering,
Kyung Hee University,
Seocheon-dong, Giheung-gu,
Yongin-si, Gyoenggi-do 446-701, Korea

Jian Wu
Department of Engineering Mechanics,
Tsinghua University,
Beijing 100084, China;
Center for Mechanics and Materials,
Tsinghua University,
Beijing 100084, China

Yonggang Huang
Department of Civil and Environmental
Engineering and Mechanical Engineering,
Northwestern University,
Evanston, IL 60208

Keh-Chih Hwang
Department of Engineering Mechanics,
Tsinghua University,
Beijing 100084, China;
Center for Mechanics and Materials,
Tsinghua University,
Beijing 100084, China

John A. Rogers
Department of Materials
Science and Engineering,
Beckman Institute, and Materials
Research Laboratory,
University of Illinois,
Urbana, IL 61801

Mechanics of Tunable Hemispherical Electronic Eye Camera Systems That Combine Rigid Device Elements With Soft Elastomers

A tunable hemispherical imaging system with zoom capability was recently developed by exploiting heterogeneous integration of rigid silicon photodetectors on soft, elastomeric supports, in designs that can facilitate tunable curvature for both the lens and detector. This paper reports analytical mechanics models for the soft materials aspects of the tunable lenses and detector surfaces used in such devices. The results provide analytical expressions for the strain distributions, apex heights and detector positions, and have been validated by the experiments and finite element analysis. More broadly, they represent important design tools for advanced cameras that combine hard and soft materials into nonplanar layouts with adjustable geometries. [DOI: 10.1115/1.4023962]

Keywords: tunable electronic eye camera, hyperelastic material, finite strain, pressure-deflection relation, analytical solution

[1]Corresponding author.
Manuscript received December 19, 2012; final manuscript received February 12, 2013; accepted manuscript posted March 6, 2013; published online August 21, 2013. Assoc. Editor: Huajian Gao.

1 Introduction

Conventional digital cameras use arrays of photodetectors in planar layouts; this configuration requires systems of lenses capable of producing images with similar geometries, thereby placing stringent constraints on engineering options, in ways that can affect cost, size, weight, and performance. Mammalian eyes provide the inspiration for alternative approaches that use curved arrays of photodetectors with geometries to match the shapes of images that form with simple, compact, low cost lenses [1–4]. Resolution scaling analyses and optical modeling [5] provide criteria for designs in such systems. Ko et al. [6] demonstrated a first, fully functional hemispherical imaging system, with configuration matched to the strongly nonplanar image surfaces (i.e., Petzval surfaces) that form with single-component, plano-convex lenses. Such "eyeball" cameras rely critically on silicon photodetectors, interconnected in mesh layouts, and supported by soft, elastomeric substrates. The result is a heterogeneous system of hard and soft materials that can be reshaped into any desired geometry, based on purely elastic deformations. In the first reported embodiments, the detector curvature was fixed [3,6], thereby rendering the cameras incompatible with changes in the nonplanar image surfaces that result from adjustable zoom. Removing this limitation requires the curvature of the detector array to change in a precise manner coordinated with the magnification setting, to ensure identical shapes for the image and detector surfaces at all zoom settings. Jung et al. [7] developed a tunable hemispherical imaging system that provides this function by using hydraulic actuation [8,9]. Here, an interconnected array of silicon photodetectors on a thin elastomeric membrane provides tunable access to a range of hemispherical shapes. Combining such a detector with a tunable lens, also controlled by fluid pressure, yields a hemispherical camera capable of adjustable zoom and excellent imaging characteristics. Such technology could be useful for night-vision surveillance, endoscopic imaging, and other areas that require compact cameras with simple zoom optics and wide angle fields of view. Related curvilinear electronic systems have been extended to other complex layouts [10,11], all of which provide function and modes of use that lie outside of the scope of possibilities provided by conventional, planar designs.

Mechanics models of these hard/soft material systems provide important insights into the design and fabrication of structures with fixed curvature [12,13]. The maximum strain in devices and their positions on a curvilinear surface can be determined analytically, and agree well with experiments [6,10,11] and with the finite element analysis (FEA) [12,13] without any parameter fitting. The objective of this paper is to establish related models and present a simple, analytical scaling relation between the overall deformation and applied pressure for tunable hemispherical imaging systems that offer adjustable zoom capabilities [7]. The results give analytically the curvatures of the lenses and detector arrays in terms of the fluid pressures, the corresponding maximum strains, and the detector positions on the tunable hemispherical surfaces. The outcomes are shown to be consistent with both the experiment and FEA.

The analytical results obtained by this study have important implications in real applications. In the tunable hemispherical imaging system, operation of the tunable electronic eye camera system requires coordinated tuning of geometries of both the lens and detector due to the intrinsic optics, while our analytical solutions can provide a very convenient tool for this purpose. During the image processing stage, analytical results can offer much faster means than finite element simulations for tracking pixel positions on the dynamically changing detector surface. This is especially important when the device is further improved for real applications and fast image processing capability is very critical. In addition, when the tunable strategy is used in other devices and systems, the analytical results can offer convenient and efficient tools for design and optimization.

2 Mechanics of Tunable Lens

2.1 Constitutive Model of PDMS Lens. Both the lenses and the photodetector arrays use the elastomer poly(dimethylsiloxane) (PDMS) as the soft material component. The stress–strain relation in PDMS is characterized by the hyperelastic model for incompressible materials [14] with the strain energy density

$$W = \sum_{k=1}^{3} C_k (I_1 - 3)^k \tag{2.1}$$

which is a function of $I_1 = \lambda_1^2 + \lambda_2^2 + \lambda_3^2$, where λ_1, λ_2, and λ_3 are the principal stretches (and $\lambda_1\lambda_2\lambda_3 = 1$ due to incompressibility), and the constants C_k are to be determined from experiments. For simple tension along direction X_1, the principal stretches are related to the nominal strain ε by $\lambda_1 = \lambda = 1 + \varepsilon$ and $\lambda_2 = \lambda_3 = 1/\sqrt{\lambda}$. For W in Eq. (2.1), the Cauchy stresses are given by [15]

$$\begin{aligned} \sigma_1 &= 2\lambda_1^2 \frac{dW}{dI_1} + p_h = 2\lambda^2 \sum_{k=1}^{3} kC_k (I_1 - 1)^{k-1} + p_h \\ \sigma_2 = \sigma_3 &= 2\lambda_2^2 \frac{dW}{dI_1} + p_h = \frac{2}{\lambda} \sum_{k=1}^{3} kC_k (I_1 - 1)^{k-1} + p_h \end{aligned} \tag{2.2}$$

where $I_1 = \lambda^2 + (2/\lambda)$, and p_h is the hydrostatic pressure and is determined from the condition of simple tension $\sigma_2 = \sigma_3 = 0$ as $p_h = -(2/\lambda) dW/dI_1$. The uniaxial stress $\sigma = \sigma_1$ is then given by

$$\begin{aligned} \sigma &= 2\left(\lambda^2 - \frac{1}{\lambda}\right)\frac{dW}{dI_1} \\ &= 2\left(\lambda^2 - \frac{1}{\lambda}\right)\left[C_1 + 2C_2(I_1 - 3) + 3C_3(I_1 - 3)^2\right] \end{aligned} \tag{2.3}$$

Figure 1 shows σ versus ε with $C_1 = 0.29$ MPa, $C_2 = 0.015$ MPa and $C_3 = 0.019$ MPa, which agrees very well with the uniaxial stress–strain curve for Sylgard 184 PDMS (10:1 mixing ratio of prepolymer and curing agent) [16]. The linear elastic modulus E can be obtained from Eq. (2.3) at the limit of infinitesimal strain ε as $E = 6C_1$, which is 1.7 MPa and is in good agreement with the literature values 2.0 MPa [6]. The shear modulus is $G = 2C_1$.

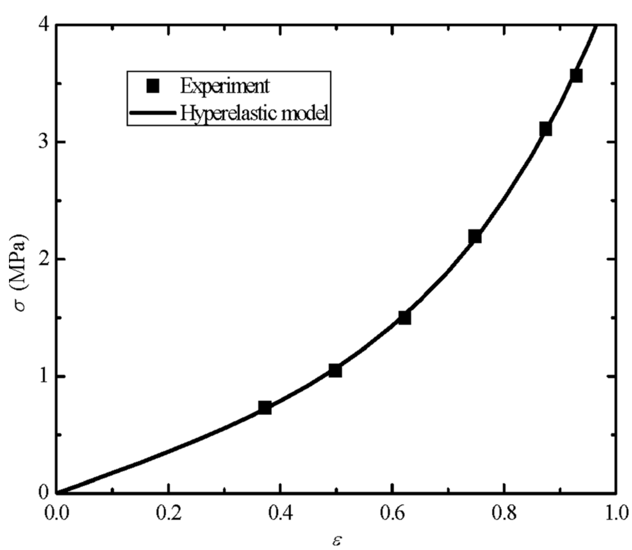

Fig. 1 The stress–strain curve for PDMS (Sylgard 184, 10:1 mixing ratio of prepolymer and curing agent) obtained from experiments [16] and from the hyperelastic model in Eq. (2.3) with the coefficients $C_1 = 0.29$ MPa, $C_2 = 0.015$ MPa, and $C_3 = 0.019$ MPa

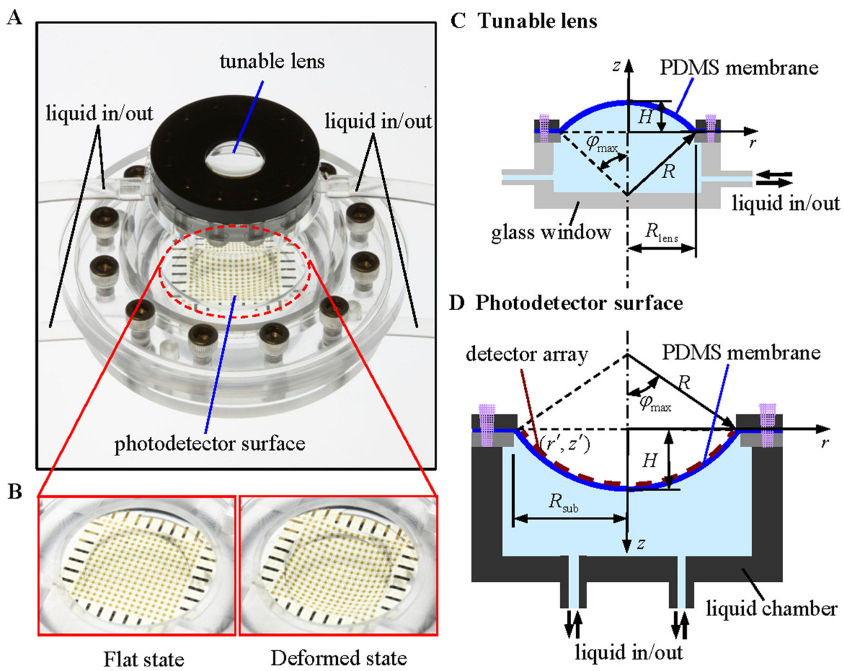

Fig. 2 **(*a*) Photograph of a camera system with a tunable lens (transparent thin PDMS membrane with $t_{lens} = 0.2$ mm thickness and $R_{lens} = 4.5$ mm radius) placed above a tunable photodetector array (16 × 16 pixels mounted on a thin PDMS membrane with $t_{sub} = 0.4$ mm thickness and $R_{sub} = 8$ mm diameter); (*b*) angled view of the photodetector surface before and after deformation; (*c*) schematic illustration of the deformation of the tunable lens due to water injection; (*d*) schematic illustration of actuating the tunable photodetector deformation via water extraction**

2.2 Deformation Analysis. Figures 2(*a*) and 2(*b*) provide the photograph of tunable lens and detector surface, respectively. The upper components correspond to an adjustable, plano-convex zoom lens, and the lower ones correspond to a tunable, hemispherical detector array. The tunable lens is made of a transparent PDMS membrane (thickness t_{lens}) filled with a liquid. The shape is initially flat and circular (radius R_{lens}), with the periphery fixed (Fig. 2(*c*)). Under pressure p, the membrane expands to a hemisphere of apex height H (Figs. 2(*a*) and 2(*c*)). The radius R and angle φ_{max} of the hemisphere (Fig. 2(*c*)) are obtained from the geometrical relations $(R-H)^2 + R_{lens}^2 = R^2$ and $\sin\varphi_{max} = R_{lens}/R$ as

$$R = \frac{R_{lens}^2 + H^2}{2H} \quad \text{and} \quad \varphi_{max} = \sin^{-1}\frac{2R_{lens}H}{R_{lens}^2 + H^2} \tag{2.4}$$

As shown in Fig. 3, FEA gives approximately a uniform strain in the meridional direction in the hemisphere, whereas details of FEA are given later. The logarithmic strain ε_r in the meridional direction is then obtained from the corresponding principal stretch λ_r, i.e., ratio of arc lengths $R\varphi_{max}$ to initial radius R_{lens}, by

$$\varepsilon_r = \ln\lambda_r = \ln\frac{R\varphi_{max}}{R_{lens}} = \ln\frac{\varphi_{max}}{\sin\varphi_{max}} \tag{2.5}$$

A ring of radius r in the initial plane of the flat PDMS becomes a ring on the hemisphere under pressure p, and has the spherical angle $\varphi = (r/R_{lens})\varphi_{max}$ and circumference $2\pi R\sin\varphi$. The logarithmic strain in the circumferential direction is then obtained from the corresponding principal stretch λ_θ, i.e., ratio of circumference $2\pi R\sin\varphi$ to $2\pi r$, by

$$\varepsilon_\theta = \ln\lambda_\theta = \ln\frac{R\sin\varphi}{r} = \ln\frac{\sin\left(\dfrac{r}{R_{lens}}\varphi_{max}\right)}{\dfrac{r}{R_{lens}}\sin\varphi_{max}} \tag{2.6}$$

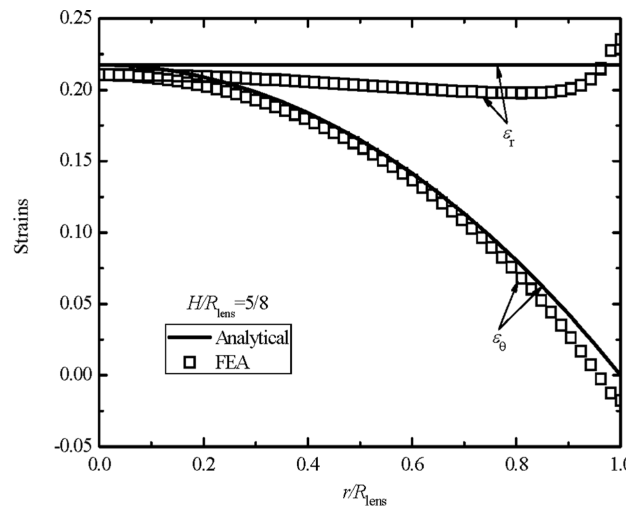

Fig. 3 **Distributions of strains in the meridional and circumferential directions in the tunable lens for an apex height $H = 5R_{lens}/8$ due to water injection**

The principal stretch in the out-of-plane direction is obtained from the incompressibility of PDMS as $\lambda_z = 1/(\lambda_r\lambda_\theta)$. Figure 3 shows the strain distributions in Eqs. (2.5) and (2.6) (versus the normalized position r/R_{lens}) for the apex height $H = 5R_{lens}/8$, which agree very well with FEA, also shown in Fig. 3. Equation (2.5) also gives the maximum strain in the membrane, which reaches 45% for a hemisphere ($H = R_{lens}$ or equivalently $\varphi_{max} = 90$ deg).

2.3 Pressure. The apex height H, or equivalently the angle φ_{max}, of the hemisphere is governed by the applied pressure p, which is the internal fluid pressure subtracted by the atmospheric pressure and is positive. Their relation is obtained analytically in the following.

The strain energy is the integration of W in Eq. (2.1) over the volume V of the hemisphere

$$\int_V W\mathrm{d}V = 2\pi t_{\text{lens}} \int_0^{R_{\text{lens}}} \sum_{k=1}^{3} C_{\text{k}}(I_1-3)^k r\mathrm{d}r = 2\pi R_{\text{lens}}^2 t_{\text{lens}} \int_0^1 \sum_{k=1}^{3} C_{\text{k}}(I_1-3)^k \bar{r}\mathrm{d}\bar{r} \tag{2.7}$$

where $\bar{r} = r/R_{\text{lens}}$, and

$$I_1 = \frac{\varphi_{\max}^2}{\sin^2\varphi_{\max}} + \frac{\sin^2(\bar{r}\varphi_{\max})}{\bar{r}^2\sin^2\varphi_{\max}} + \frac{\bar{r}^2\sin^4\varphi_{\max}}{\varphi_{\max}^2\sin^2(\bar{r}\varphi_{\max})} \tag{2.8}$$

The variation of strain energy is $2\pi R_{\text{lens}}^2 t_{\text{lens}} \int_0^1 \sum_{k=1}^{3} kC_{\text{k}}(I_1-3)^{k-1}\partial I_1/\partial\varphi_{\max}\bar{r}\mathrm{d}\bar{r}\delta\varphi_{\max}$, which equals to the virtual work done by the applied pressure, $p\delta[\pi/6(3R_{\text{lens}}^2H+H^3)] = (\pi/2)p(R_{\text{lens}}^2+H^2)\delta H$, where $\pi/6(3R_{\text{lens}}^2H+H^3)$ is the volume of the hemisphere, and δH is related to $\delta\varphi_{\max}$ via Eq. (2.4). These give the applied pressure, normalized by $Gt_{\text{lens}}/R_{\text{lens}}$, in terms of $\varphi_{\max}$ as

$$\frac{pR_{\text{lens}}}{Gt_{\text{lens}}} = (1+\cos\varphi_{\max})^2 \int_0^1 \sum_{k=1}^{3} k\frac{C_{\text{k}}}{C_1}(I_1-3)^{k-1}\frac{\partial I_1}{\partial\varphi_{\max}}\bar{r}\mathrm{d}\bar{r} \tag{2.9}$$

where $G = 2C_1$ is the shear modulus. The normalized apex height H/R_{lens} is related to $\varphi_{\max}$ via Eq. (2.4), and therefore depends only on the normalized pressure $pR_{\text{lens}}/(Gt_{\text{lens}})$ (and C_2/C_1 and C_3/C_1).

2.4 Prestrain. Fabrication of the membrane and its integration onto the stage (Fig. 2(*c*)) involves a compressive prestrain ε_0 (e.g., -2% in the experiment) prior to the applied pressure [7]. For the membrane with radius R_{lens} on the stage, the natural radius prior to prestrain is $R_{\text{lens}}/(1+\varepsilon_0)$. The principal stretches, accounting for the effect of prestrain, are

$$\lambda_{\text{r}} = \frac{R\varphi_{\max}}{R_{\text{lens}}/(1+\varepsilon_0)} = (1+\varepsilon_0)\frac{\varphi_{\max}}{\sin\varphi_{\max}}$$
$$\lambda_\theta = \frac{R\sin\varphi}{r/(1+\varepsilon_0)} = (1+\varepsilon_0)\frac{\sin\left(\frac{r}{R_{\text{lens}}}\varphi_{\max}\right)}{\frac{r}{R_{\text{lens}}}\sin\varphi_{\max}} \tag{2.10}$$

and $\lambda_{\text{z}} = 1/(\lambda_{\text{r}}\lambda_\theta)$. The applied pressure in Eq. (2.9) becomes

$$\frac{pR_{\text{lens}}}{Gt_{\text{lens}}} = \left(\frac{1+\cos\varphi_{\max}}{1+\varepsilon_0}\right)^2 \int_0^1 \sum_{k=1}^{3} k\frac{C_{\text{k}}}{C_1}(I_1-3)^{k-1}\frac{\partial I_1}{\partial\varphi_{\max}}\bar{r}\mathrm{d}\bar{r} \tag{2.11}$$

where

$$I_1 = (1+\varepsilon_0)^2\left[\frac{\varphi_{\max}^2}{\sin^2\varphi_{\max}} + \frac{\sin^2(\bar{r}\varphi_{\max})}{\bar{r}^2\sin^2\varphi_{\max}} + \frac{\bar{r}^2\sin^4\varphi_{\max}}{(1+\varepsilon_0)^6\varphi_{\max}^2\sin^2(\bar{r}\varphi_{\max})}\right] \tag{2.12}$$

The normalized apex height H/R_0, which is related to $\varphi_{\max}$ via Eq. (2.4), now depends on the normalized pressure $pR_{\text{lens}}/(Gt_{\text{lens}})$ and prestrain ε_0 (also C_2/C_1 and C_3/C_1) via Eqs. (2.11) and (2.12). Figure 4 shows the normalized apex height, H/R_{lens}, versus the normalized pressure, $pR_{\text{lens}}/(Gt_{\text{lens}})$, for the prestrain $\varepsilon_0 = 0$ and -2%, and latter agrees very well with the experiments for $R_{\text{lens}} = 4.5$ mm and $t_{\text{lens}} = 0.2$ mm [7]. Results from linear elastic model are also shown in Fig. 4 for comparison. For linear elastic model, the elastic strain energy is given as $U_{\text{linear}} = \pi Et/(1-\nu^2)\int_0^{R_0}(\varepsilon_r^2+\varepsilon_\theta^2+2\nu\varepsilon_r\varepsilon_\theta)r\mathrm{d}r$, where ε_r and ε_θ were given in Eqs. (2.5) and (2.6), the Young's modulus is $E = 6C_1 = 0.17$ MPa, and the Poisson's ratio is taken as $\nu = 0.48$. As shown in Fig. 4, for small normalized pressure, the linear elastic model can predict the normalized apex height fairly accurately. However, when normalized pressure becomes large, the linear elastic model deviates from the experiment significantly.

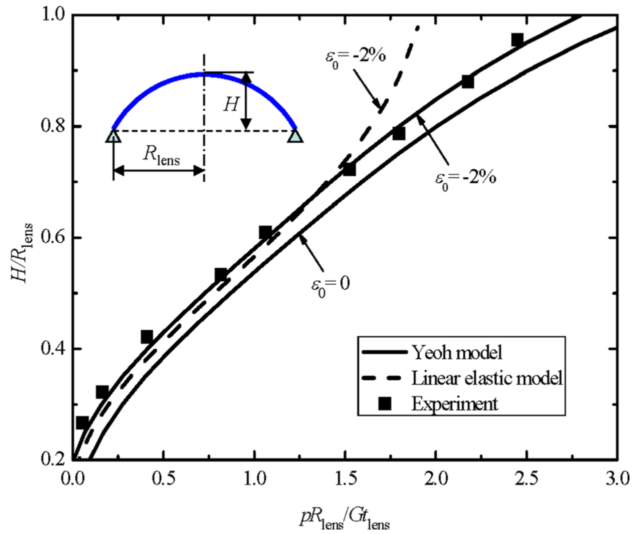

Fig. 4 Normalized apex height H/R_{lens} of the tunable lens versus the normalized applied pressure $pR_{\text{lens}}/(Gt_{\text{lens}})$ due to water injection, where R_{lens} and t_{lens} are the radius and thickness of the lens, respectively, and G is the shear modulus. The prestrain in the lens is $\varepsilon_0 = 0$, and -2% as in experiments [7].

2.5 Finite Element Analysis. Three-dimensional finite element analysis (FEA) is used to study the deformation of the tunable lens due to water injection. The tunable lens is modeled as a hyperelastic membrane with the material properties obtained in Sec. 2.1. The membrane (with 0.2 mm thickness and 4.5 mm radius) is fixed at the periphery, and a uniform pressure is applied on the bottom surface (Fig. 2(*c*)) of the membrane. The continuum shell element SC8R in the ABAQUS package [17] is used to model the hyperelastic membrane. For the apex height of the membrane $H = 5R_{\text{lens}}/8$, the meridional and circumferential strains obtained by FEA are shown in Fig. 3.

3 Mechanics of Tunable Detector Surface

3.1 Deformation Analysis. Figure 2(*b*) shows a tunable, hemispherical detector array on initially flat PDMS substrate (thickness t_{sub} and radius R_{sub}) with the periphery fixed (Fig. 2(*d*)), which expands to a hemisphere of apex height H (Figs. 2(*b*) and 2(*d*)) under the applied pressure p, which is the atmospheric pressure subtracted by the internal fluid pressure and is positive. Similar to Eq. (2.4), the radius R and angle $\varphi_{\max}$ of the hemisphere (Fig. 2(*d*)) satisfy

$$R = \frac{R_{\text{sub}}^2+H^2}{2H} \quad \text{and} \quad \varphi_{\max} = \sin^{-1}\frac{2R_{\text{sub}}H}{R_{\text{sub}}^2+H^2} \tag{3.1}$$

Let l_{detector} and l_{space} denote the detector size and spacing, respectively, which give the fill factor (areal fraction of detectors) $f = l_{\text{detector}}^2/(l_{\text{detector}}+l_{\text{space}})^2$. On the average the total length of detectors is fR_{sub} across the initial radius R_{sub}, and that of PDMS (uncovered by detectors) is $(1-f)R_{sub}$. The stretch of PDMS underneath the detectors is negligible since the tensile stiffness of the silicon photodetectors is several orders of magnitude larger than that of PDMS (e.g., 0.16 MPa · m for silicon detector (thickness 1.2 μm and Young's modulus 130 GPa) and 0.80kPa · m for PDMS (thickness 0.4 mm and Young's modulus 2 MPa) as in experiments [7]. Therefore, its length fR_{sub} remains essentially the same during the expansion due to applied pressure p, and the length $(1-f)R_{sub}$ of PDMS uncovered by the detectors expands to $R\varphi_{max} - fR_{sub}$. This gives the principal stretches of PDMS uncovered by the detectors as

$$\lambda_r = \frac{R\varphi_{max} - fR_{sub}}{(1-f)R_{sub}} = \frac{1}{1-f}\left(\frac{\varphi_{max}}{\sin\varphi_{max}} - f\right)$$
$$\lambda_\theta = \frac{R\sin\varphi - fr}{(1-f)r} = \frac{1}{1-f}\left[\frac{\sin\left(\frac{r}{R_{sub}}\varphi_{max}\right)}{\frac{r}{R_{sub}}\sin\varphi_{max}} - f\right] \tag{3.2}$$

and $\lambda_z = 1/(\lambda_r\lambda_\theta)$.

Fabrication of the detectors onto the stage (Fig. 2(*d*)) involves a tensile prestrain ε_0 (e.g., 2% in the experiment) prior to the applied pressure [7]. The principal stretches, accounting for the effect of prestrain, are

$$\lambda_r = \frac{1+\varepsilon_0}{1-f}\frac{\varphi_{max}}{\sin\varphi_{max}} - \frac{f}{1-f}$$
$$\lambda_\theta = \frac{1+\varepsilon_0}{1-f}\frac{\sin\left(\frac{r}{R_{sub}}\varphi_{max}\right)}{\frac{r}{R_{sub}}\sin\varphi_{max}} - \frac{f}{1-f} \tag{3.3}$$

and $\lambda_z = 1/(\lambda_r\lambda_\theta)$.

3.2 Pressure. The strain energy is the integration of strain energy density in Eq. (2.1) over the volume of PDMS uncovered by the detectors as $2\pi(1-f)R_{sub}^2/(1+\varepsilon_0)^2 t_{sub}\int_0^1 \sum_{k=1}^{3} C_k(I_1-3)^k \bar{r}\,d\bar{r}$, where

$$I_1 = \left(\frac{1+\varepsilon_0}{1-f}\frac{\varphi_{max}}{\sin\varphi_{max}} - \frac{f}{1-f}\right)^2 + \left[\frac{1+\varepsilon_0}{1-f}\frac{\sin(\bar{r}\varphi_{max})}{\bar{r}\sin\varphi_{max}} - \frac{f}{1-f}\right]^2 + \left(\frac{1+\varepsilon_0}{1-f}\frac{\varphi_{max}}{\sin\varphi_{max}} - \frac{f}{1-f}\right)^{-2}\left[\frac{1+\varepsilon_0}{1-f}\frac{\sin(\bar{r}\varphi_{max})}{\bar{r}\sin\varphi_{max}} - \frac{f}{1-f}\right]^{-2} \tag{3.4}$$

The principle of virtual work gives the applied pressure, normalized by Gt_{sub}/R_{sub}, as

$$\frac{pR_{sub}}{Gt_{sub}} = (1-f)\left(\frac{1+\cos\varphi_{max}}{1+\varepsilon_0}\right)^2 \int_0^1 \sum_{k=1}^{3} k\frac{C_k}{C_1}(I_1-3)^{k-1}\frac{\partial I_1}{\partial\varphi_{max}}\bar{r}\,d\bar{r} \tag{3.5}$$

It degenerates to Eq. (2.11) for lens in the limit of $f=0$. The normalized apex height H/R_{sub}, related to φ_{max} via Eq. (3.1), depends on the normalized pressure $pR_{sub}/(Gt_{sub})$, fill factor f of detectors, and prestrain ε_0 (and C_2/C_1 and C_3/C_1). Figure 5 shows the normalized apex height, H/R_{sub}, versus the normalized pressure, $pR_{sub}/(Gt_{sub})$, for the prestrain $\varepsilon_0 = 0$ and 2%, and latter agrees very well with the experiments for $R_{sub} = 8.0$ mm, $t_{sub} = 0.4$ mm and fill factor $f = 30\%$ ($l_{detector} = 0.5$ mm and $l_{space} = 0.42$ mm) [7].

Figure 6 shows the normalized apex height, H/R_{sub}, versus the normalized pressure, $pR_{sub}/(Gt_{sub})$, for the fill factor $f = 0$, 30%, and 60% without prestrain ($\varepsilon_0 = 0$). As f increases, the apex height decreases rapidly because the stiff detectors can significantly increase the system stiffness.

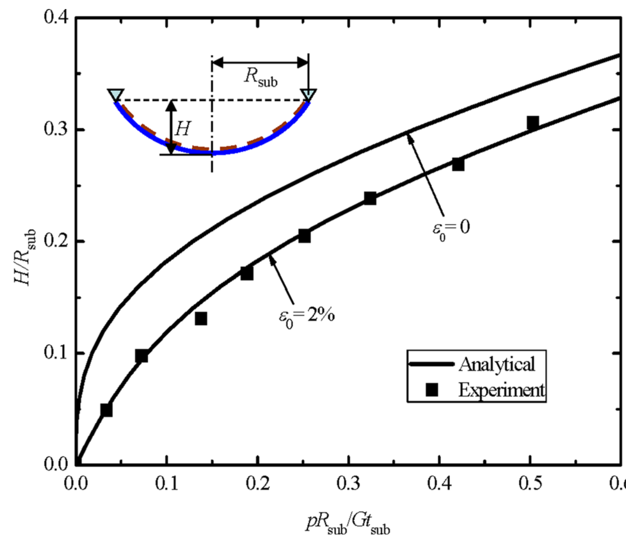

Fig. 5 Normalized apex height H/R_{sub} of the tunable detector surface versus the normalized applied pressure $pR_{sub}/(Gt_{sub})$ due to water extraction, where R_{sub} and t_{sub} are the radius and thickness of PDMS substrate for the detectors, respectively, and G is the shear modulus. The fill factor of detectors is $f = 30\%$ as in experiments [7]. The prestrain is $\varepsilon_0 = 0$ and 2% in the PDMS substrate.

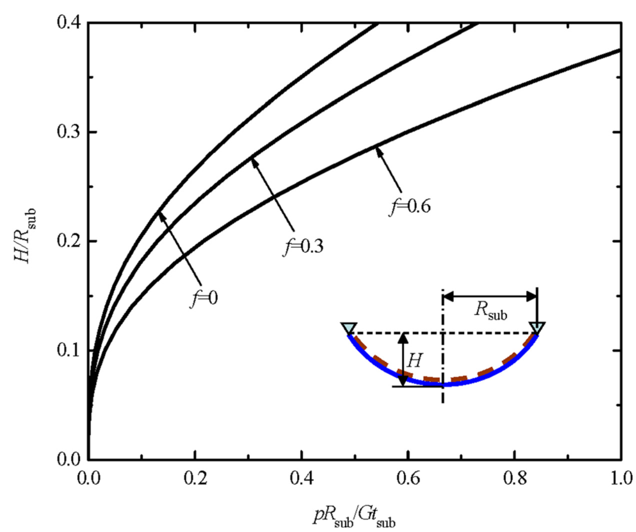

Fig. 6 Normalized apex height H/R_{sub} of the tunable detector surface versus the normalized applied pressure $pR_{sub}/(Gt_{sub})$ due to water extraction, where R_{sub} and t_{sub} are the radius and thickness of PDMS substrate for the detectors, respectively, and G is the shear modulus. The fill factor of detectors is $f = 0$, 30%, and 60%. The prestrain is $\varepsilon_0 = 0$ in the PDMS substrate.

3.3 Detector Positions. A simple but accurate method is established in this section to determinate the detector positions on the hemispherical surface under applied pressure in the tunable imaging system. Let (r, θ, z) denote the cylindrical coordinates with the origin at the center of flat surface of the PDMS substrate prior to applied pressure p. Section 3.1 suggests that the cylindrical angle θ of any detector remains the same when the detector surface expands to the hemisphere. Any defector with radius r to the center has the axial and radial coordinates (r', z') on the hemisphere after the deformation, where

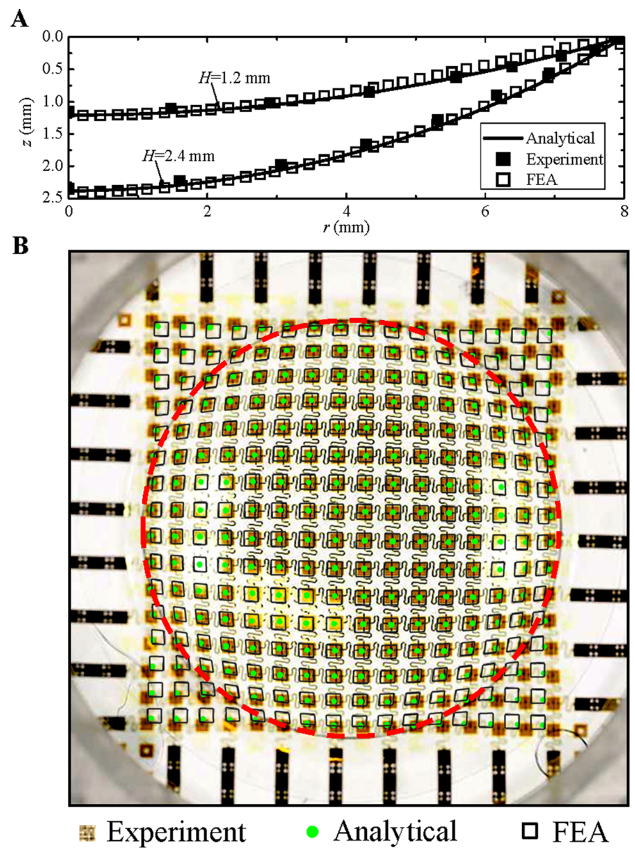

Fig. 7 (*a*) Side view of the deformed profiles of detector surface at different stages of water extraction (apex height $H = 1.2$ mm and 2.4 mm). (*b*) Top view of the detector positions for an apex height $H = 2.87$ mm. The radius and thickness of PDMS substrate is $R_{sub} = 8$ mm and $t_{sub} = 0.4$ mm, and the fill factor of detectors and prestrain are $f = 30\%$ and $\varepsilon_0 = 2\%$, respectively, as in experiments [7].

$$
\begin{aligned}
r' &= R\sin\left(\frac{r}{R_{sub}}\varphi_{max}\right) = \frac{R_{sub}^2 + H^2}{2H}\sin\left[\frac{r}{R_{sub}}\sin^{-1}\left(\frac{2R_{sub}H}{R_{sub}^2 + H^2}\right)\right] \\
z' &= R\left[\cos\left(\frac{r}{R_{sub}}\varphi_{max}\right) - \cos\varphi_{max}\right] \\
&= \frac{R_{sub}^2 + H^2}{2H}\left\{\cos\left[\frac{r}{R_{sub}}\sin^{-1}\left(\frac{2R_{sub}H}{R_{sub}^2 + H^2}\right)\right] - \frac{R_{sub}^2 - H^2}{R_{sub}^2 + H^2}\right\}
\end{aligned}
\tag{3.6}
$$

The periphery of the substrate $r = R_{sub}$ remains the same ($r' = R_{sub}, z' = 0$) while the center $r = 0$ becomes ($r' = 0, z' = H$) on the hemisphere, where the apex height H is related to the applied pressure p via Eq. (3.5) (also Figs. 5 and 6). The PDMS substrate (with 0.4 mm thickness and 8 mm radius) is modeled by the same element SC8R in the ABAQUS package [17] to study the deformation of tunable eye due to water extraction. The analytically obtained detector positions, shown by green dots in Fig. 7, agrees very well with both the experiment (filled square) and FEA (open square); with the side view (z versus r) in Fig. 7(*a*) for $R_{sub} = 8$ mm, $H = 1.2$ mm and $H = 2.4$ mm [7], and top view given in Fig. 7(*b*) for $R_{sub} = 8$ mm and $H = 2.87$ mm as in experiments. These excellent agreements further validate analytical model. As shown in Fig. 7(*b*), positions of photodetectors near the clamped edge deviate from the experiment, especially in the four corner regions outside the red dashed circle. In the experiment, the four corners outside of the red dashed circle is compressed by two confinement elements, and remain flat when the area inside the circle is deformed by the applied pressure. The significant deviation of

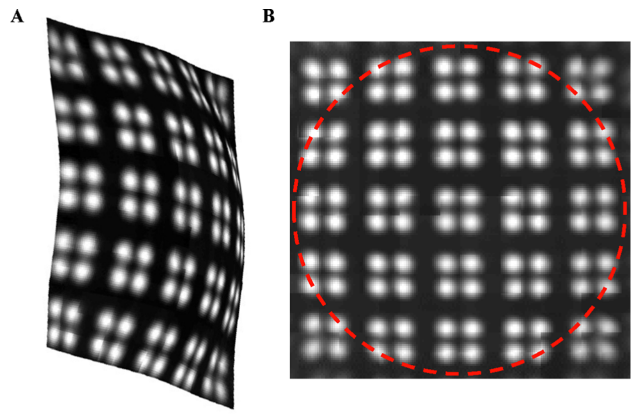

Fig. 8 The images of an array of bright circular discs, captured at the state of $R = 17.8$ mm, $R_{lens} = 6.9$ mm, and distance between lens and detector is 27.3 mm. (*a*) 3D rendering of the image on the hemispherical detector surface, (*b*) Planar projection of the image in (*a*).

photodetector positions in the four corner regions is probably due to the excessive pressure applied by the two confinement elements to ensure good sealing of the water chamber. However, photodetectors in the four corner regions do not contribute to effective imaging of the tunable electronic eye camera, since they remain flat. For photodetectors within the red dashed circle, position deviation is relatively small, and does not significantly affect the image quality. The analytical prediction of photodetector positions was used to construct images in the experiment and showed very good results. As shown in Fig. 8, the images of an array of bright circular discs, captured at the state of $R = 17.8$ mm, $R_{lens} = 6.9$ mm, and distance between lens and detector 27.3 mm, shows very good quality.

4 Concluding Remarks

Analytical models for hydraulically tunable lenses and arrays of photodetectors are established in Secs. 2 and 3, respectively. The results give analytical expressions for the strain distributions, apex heights and detector positions for any applied pressure, in a manner consistent with determinations by the experiment and finite element analysis. The outcomes provide important design tools for tunable hemispherical imaging systems as well as other related advanced electronic and optoelectronic systems that combine hard device elements with soft, elastomeric supports.

Acknowledgment

C.L. acknowledges the support from NSFC under Grant No. 11172263. The mechanics and materials components of the work were supported by the National Science Foundation under Grant Nos. ECCS-0824129 and OISE-10 and by DARPA Contract No. N66001-10-1-4008 and by Sharp Corporation. Y.H. also acknowledges the support from NSFC.

References

[1] Dinyari, R., Rim, S. B., Huang, K., Catrysse, P. B., and Peumans, P., 2008, "Curving Monolithic Silicon for Nonplanar Focal Plane Array Applications," Appl. Phys. Lett., **92**(9), p. 091114.

[2] Rim, S. B., Catrysse, P. B., Dinyari, R., Huang, K., and Peumans, P., 2008, "The Optical Advantages of Curved Focal Plane Arrays," Opt. Express, **16**(7), pp. 4965–4971.

[3] Xu, X., Davanco, M., Qi, X. F., and Forrest, S. R., 2008, "Direct Transfer Patterning on Three Dimensionally Deformed Surfaces at Micrometer Resolutions and Its Application to Hemispherical Focal Plane Detector Arrays," Org. Electron., **9**(6), pp. 1122–1127.

[4] Dumas, D., Fendler, M., Berger, F., Cloix, B., Pornin, C., Baier, N., Druart, G., Primot, J., and le Coarer, E., 2012, "Infrared Camera Based on a Curved Retina," Opt. Lett., **37**(4), pp. 653–655.

[5] Cossairt, O. S., Miau, D., and Nayar, S. K., 2011, "Scaling Law for Computational Imaging Using Spherical Optics," J. Opt. Soc. Am. A, **28**(12), pp. 2540–2553.
[6] Ko, H. C., Stoykovich, M. P., Song, J. Z., Malyarchuk, V., Choi, W. M., Yu, C. J., Geddes, J. B., Xiao, J. L., Wang, S. D., Huang, Y. G., and Rogers, J. A., 2008, "A Hemispherical Electronic Eye Camera Based on Compressible Silicon Optoelectronics," Nature, **454**(7205), pp. 748–753.
[7] Jung, I. W., Xiao, J. L., Malyarchuk, V., Lu, C. F., Li, M., Liu, Z. J., Yoon, J., Huang, Y. G., and Rogers, J. A., 2011, "Dynamically Tunable Hemispherical Electronic Eye Camera System With Adjustable Zoom Capability," Proc. Natl. Acad. Sci. U. S. A., **108**(5), pp. 1788–1793.
[8] Schneider, F., Mueller, C., and Wallrabe, U., 2008, "A Low Cost Adaptive Silicone Membrane Lens," J. Opt. A, Pure Appl. Opt., **10**(4), p. 044002.
[9] Sanchez-Perez, J. R., Boztug, C., Chen, F., Sudradjat, F. F., Paskiewicz, D. M., Jacobson, R. B., Lagally, M. G., and Paiella, R., 2011, "Direct-Bandgap Light-Emitting Germanium in Tensilely Strained Nanomembranes," Proc. Natl. Acad. Sci. U. S. A., **108**(47), pp. 18893–18898.
[10] Ko, H. C., Shin, G., Wang, S. D., Stoykovich, M. P., Lee, J. W., Kim, D. H., Ha, J. S., Huang, Y. G., Hwang, K. C., and Rogers, J. A., 2009, "Curvilinear Electronics Formed Using Silicon Membrane Circuits and Elastomeric Transfer Elements," Small, **5**(23), pp. 2703–2709.
[11] Shin, G., Jung, I., Malyarchuk, V., Song, J. Z., Wang, S. D., Ko, H. C., Huang, Y. G., Ha, J. S., and Rogers, J. A., 2010, "Micromechanics and Advanced Designs for Curved Photodetector Arrays in Hemispherical Electronic-Eye Cameras," Small, **6**(7), pp. 851–856.
[12] Wang, S. D., Xiao, J. L., Jung, I., Song, J. Z., Ko, H. C., Stoykovich, M. P., Huang, Y. G., Hwang, K. C., and Rogers, J. A., 2009, "Mechanics of Hemispherical Electronics," Appl. Phys. Lett., **95**(18), p. 181912.
[13] Wang, S., Xiao, J., Song, J., Ko, H. C., Hwang, K.-C., Huang, Y., and Rogers, J. A., 2010, "Mechanics of Curvilinear Electronics," Soft Matter, **6**(22), pp. 5757–5763.
[14] Yeoh, O. H., 1993, "Some Forms of the Strain-Energy Function for Rubber," Rubber Chem. Technol., **66**(5), pp. 754–771.
[15] Rivlin, R. S., 1948, "Large Elastic Deformations of Isotropic Materials. 4. Further Developments of the General Theory," Philos. Trans. R. Soc. London, Ser. A, **241**(835), pp. 379–397.
[16] Schneider, F., Fellner, T., Wilde, J., and Wallrabe, U., 2008, "Mechanical Properties of Silicones for MEMS," J. Micromech. Microeng., **18**(6), p. 065008.
[17] ABAQUS, 2009 *Analysis User's Manual, Vl. 6.9*, Dassault Systèmes, Pawtucket, RI.